Received: 13 July 2017 | Revised: 17 November 2017 | Accepted: 30 January 2018

DOI: 10.1002/we.2185

RESEARCH ARTICLE

WILEY

Sound propagation through the wake flow of a hilltop wind turbine—A numerical study

Dietrich Heimann | Antonia Englberger | Arthur Schady

Deutsches Zentrum für Luft- und Raumfahrt e.V., Institut für Physik der Atmosphäre, Oberpfaffenhofen, Weßling, Germany

Correspondence
Dr Arthur Schady, Deutsches Zentrum für Luft- und Raumfahrt e.V., Institut für Physik der Atmosphäre, Oberpfaffenhofen, Weßling 82234, Germany.
Email: arthur.schady@dlr.de

Funding information
German Federal Ministry for Economic Affairs and Energy, Grant/Award Number: 0325518

Abstract

The sound propagation from a wind turbine situated on the top of a hill into the downwind domain is studied by numerical simulations for 13 cases with varying hill geometry and inflow conditions. The influence of the hill on the atmospheric flow and the wake due to the rotor are simulated by precursory large-eddy simulations. In addition to the combined consideration of hill and turbine wake effects, these effects are also separately evaluated. The results show that placing the turbine on top of a hill leads to slightly lower sound levels on the downwind plane, although the wake alone supports downward refraction and tends to increase the sound impact near the ground at greater distance. Variations of the hill geometry and the inflow conditions do not have significant effects on the near-ground sound levels in the downwind domain.

KEYWORDS

hill, numerical simulation, sound propagation, wake flow, wind turbine

1 | INTRODUCTION

When operating, wind energy converters emit sound which is mostly produced by the interaction between the rotating blades and the turbulent air that impinges on and flows around the blades (aerodynamic noise; eg, Kim et al[1]). Further sound is produced by the gear (if existing) and diverse auxiliary drives to control yaw and pitch. The problems of wind turbine noise in the environment (emission, propagation, impact on human health) are summarized by Rogers et al[2] or Tabassum-Abbasi et al.[3] The perception of wind turbine noise by people (annoyance) is addressed, for instance, by Pedersen et al.[4] The local impact of noise depends not only on the sound emission at the turbine but also on the propagation of the sound waves through the atmosphere. Both emission and propagation are determined by the inflow condition (wind profile, temperature stratification, and turbulence) and the operating condition of the turbine. The propagation is additionally influenced by the specific wake due to the moving rotor blades, eg, Vermeer et al,[5] and the underlying ground. The wake structure was investigated by Lidar measurements, eg, Bingöl et al,[6] Trujillo et al,[7] and Käsler et al,[8] and numerical simulations, eg, Wussow et al,[9] Jimenez et al,[10] Troldborg et al,[11] Gross,[12] Sørensen et al,[13] or Gebraad et al.[14]

Only recently have simulations been published that consider the influence of the wake flow in the predicting the far-field sound from wind converters. Heimann et al[15] used a 3-dimensional ray-based model which was coupled to 2 different Reynolds-averaged numerical flow models. They found that the sound impact is very sensitive to details in the meteorological fields. Lee et al[16] used a 2-dimensional diagnostic wave-based propagation model with axisymmetric approximation and successfully compared the results with measurements. Barlas et al[17] studied the influence of the wake on the sound impact above plane ground. They used a 2-dimensional wave-based sound propagation model that was coupled with a large-eddy simulation (LES) of the air flow. It turned out that during stable stratification, the sound level can be strongly underestimated if the turbine wake is not considered. However, all these examples refer to plane ground.

To optimize the exploitation of wind energy, wind turbines are often placed where the wind speed is high. It is known that atmospheric airflow over gentle orography causes an increased wind speed above the crest of a ridge or the top of a hill. An early review of this behaviour was provided by Corby.[18] The importance for wind energy was also recognized[19] already at that time. Since the 1970s, numerical simulations of the airflow above hills became available (eg, Taylor[20]). The growing demand for wind energy gave rise to more detailed investigations of the airflow over hills, its impact on the wind energy potential, and consequences to the wake flow. Comprehensive surveys of this kind were the Askervein Hill Project[21] in 1982/1983 and the Bolund Experiment[22,23] in 2007/2008. A further field experiment was planned within the NEWA project[24] and conducted in 2017 near Perdigão/Portugal.

Wind turbine noise from a facility on top of a hill or ridge has not been widely studied, so far. Prospathopoulos and Voutsinas[25] showed that the complex terrain has an impact on the sound level in the vicinity of wind turbines. Besides measurements, they used a ray model, but horizontal variations of the wind were not accounted for. Most recently, Van Renterghem[26] has used a hybrid method with analytical solutions in combination with a parabolic equation model to simulate the sound propagation from a ridge-top wind turbine across a valley. However, effects of the hill and the turbine on the atmosphere have not been considered in this study. Instead, the study is confined to the effects of the terrain curvature and ground impedance on sound reflection.

The present paper considers a wind turbine on top of a 3-dimensional hill. In addition to previous studies, it investigates the complete process chain from the undisturbed inflow, its orographically induced modification by the hill, the disturbed flow in the wake of a turbine on top of the hill, to the sound propagation through the correspondingly modified atmosphere. The study is based on numerical simulations by coupling a large-eddy flow model (LES model) as precursor model to a ray-based sound particle model. It is the goal to elucidate the specific influences of the hill geometry, ground surface characteristics and large-scale conditions on the turbulent air flow in the lee of hill and turbine, the respective sound propagation, and the resulting sound impact near the ground.

The general layout of the numerical experimentation is explained in Section 2. The flow model and its results are presented in Section 3. Section 4 presents the acoustical simulations. Results are discussed in Section 5. Eventually, conclusions follow in Section 6.

2 | GENERAL LAYOUT

The study deals with a 3-blade horizontal-axis wind turbine with a hub height of z_{hub} = 100 m above ground and an upwind rotor with a radius of r = 50 m. The turbine is assumed to stand on top of a 50 m high axisymmetric hill centred at (x_0, y_0) with a Witch-of-Agnesi slope profile:

$$h(x,y) = \frac{H}{\left(\frac{x-x_0}{L}\right)^2 + \left(\frac{y-y_0}{L}\right)^2 + 1}, \tag{1}$$

where h is the terrain elevation, H = 50 m the hill height, $x_0 = y_0 = 0$ is the horizontal position of the hilltop in the origin of the Cartesian coordinate system x, y, z, and L is the horizontal scale that determines the steepness of the slope (and thus the maximum slope angle φ). L corresponds to the half width at half maximum of the hill. The position of the wind turbine on top of the hill is illustrated as a cross-section along the x-axis in Figure 1. In the following, the horizontal distance between any location (x, y, z) and the position of the turbine $(0, 0)$ is denoted as $s = (x^2 + y^2)^{1/2}$.

All cases are initialized with a neutrally stratified background atmosphere with a linear temperature profile

$$T_b(z) = T_b(z_0) - \frac{g}{c_p}(z - z_0), \tag{2}$$

where g is the gravity acceleration and c_p the specific heat capacity at constant pressure. The resulting vertical temperature gradient is approx. $\partial T_b/\partial z = -9.76 \cdot 10^{-3}$ K/m. The corresponding undisturbed inflow (background) wind profile is logarithmic:

$$u_b(z) = \frac{u_*}{\kappa}\ln\left(\frac{z}{z_0}\right), \tag{3}$$

with the mean wind component in x-direction u_b, the friction velocity u_*, the roughness length of the ground surface z_0, and the von-Karman constant κ = 0.4.

In total, 13 experimental cases with varying inflow conditions and a varying steepness of the hill are considered. The parameter setting of all cases is summarized in Table 1. The following dependencies are investigated, regarding the impact of

- the steepness of the hill (S1, S2, S3), controlled by L in Equation 1,
- the wind velocity at the rotor (S4, S5), controlled by z_0 in Equation 3,
- the velocity shear between top tip and bottom tip (S6, S7), controlled by u_* in Equation 3, and
- the turbulence level α of the background flow (S8, S9), cf Section 3.

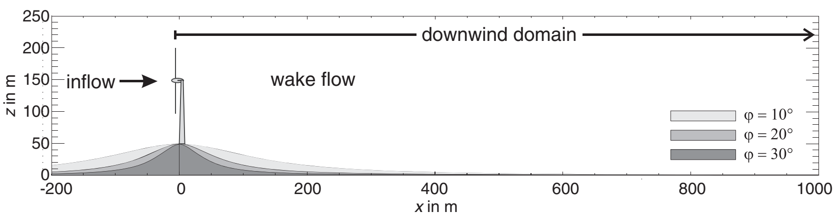

FIGURE 1 Vertical cross-section along the x-axis (at $y = y_0$) showing the position of the wind turbine on top of a 50-m-high hill. The 3 terrain profiles are grey shaded (cf Table 1)

TABLE 1 Overview of the cases

Case	Wind Turbine	Rotational Speed, min^{-1}	H, m	φ, deg	L, m	u_*, m/s	u_b at Hub Height, m/s	z_o, m	Turbulence Level α
S0.1	Yes	10.4	0	0		0.45	7.8	0.1	10
S0.2	Yes	10.4	0	0		0.45	8.6	0.05	10
S0.3	Yes	10.4	0	0		0.45	7.0	0.2	10
S1.0	No		50	10	184.3	0.45	7.8	0.1	10
S1	Yes	11.0	50	10	184.3	0.45	7.8	0.1	10
S2	Yes	11.0	50	20	89.3	0.45	7.8	0.1	10
S3	Yes	11.0	50	30	56.3	0.45	7.8	0.1	10
S4	Yes	12.0	50	20	89.3	0.45	8.6	0.05	10
S5	Yes	9.9	50	20	89.3	0.45	7.0	0.2	10
S6	Yes	7.2	50	20	89.3	0.30	5.2	0.1	10
S7	Yes	14.7	50	20	89.3	0.60	10.4	0.1	10
S8	Yes	11.0	50	20	89.3	0.45	7.8	0.1	5
S9	Yes	11.0	50	20	89.3	0.45	7.8	0.1	20

The parameters are used in Equations 1 and 3.

In addition, S1.0 represents a reference case with a hill, but without a wind turbine on top. Case S1.0 is used to demonstrate the sound propagation from a fictive wind turbine through the orographically modified air flow without a turbine-induced wake. S0.1, S0.2, and S0.3 are further reference cases without a hill but with a wind turbine and different values of z_0. These cases demonstrate the sound propagation from a wind turbine through the turbine-induced wake without orographic modifications.

3 | FLOW SIMULATIONS

An inviscid and incompressible flow through a wind turbine on top of a hill is simulated with the multiscale geophysical flow solver EULAG.[27] The numerical model EULAG is at least second-order accurate in time and space and is well suited for massively-parallel computations. A comprehensive description and discussion of the geophysical flow solver EULAG can be found in Smolarkiewicz and Margolin[28] and Prusa et al.[27]

For the LESs conducted herein, the Boussinesq approximated equations of motion and continuity[29] for a neutrally stratified flow

$$\frac{dV}{dt} = -G\nabla\frac{p'}{\rho_0} + \frac{F}{\rho_0} + \varepsilon, \tag{4}$$

$$\nabla\cdot(\rho_0\bar{G}V) = 0, \tag{5}$$

with constant density ρ_0 = 1.1 kg m^{-3} are solved for the Cartesian velocity components $V = (u, v, w)$. In Equations 4 and 5, d/dt, ∇, and $\nabla\cdot$ represent the total derivative, the gradient, and the divergence in terrain-following coordinates, respectively. The subgrid-scale term ε symbolizes viscous dissipation.

The quantity p' represents the pressure perturbation with respect to p_0. The metric coefficient G and the Jacobian of the transformation $\bar{G}$ stand for geometric terms that result from the general coordinate transformation into nonorthogonal terrain-following coordinates.[27,30-32] F represents additional external forces related to the parametrization of the wind turbine in the numerical model EULAG.

In general, the geophysical flow solver EULAG owes its versatility to a unique design that combines a rigorous theoretical formulation in generalized curvilinear coordinates[31] with nonoscillatory forward-in-time differencing for fluids built on the multidimensional positive definite advection transport algorithm (MPDATA), which is based on the convexity of upwind advection and a robust, exact-projection type, elliptic Krylov solver.[27,28]

Here, LESs of the flow through a wind turbine on top of a hill are conducted with a turbulent kinetic energy (TKE) closure.[33,34] The simulations are performed for different inflow conditions and hill structures lasting 20 minutes on 512 × 64 × 64 grid points with a horizontal and vertical resolution of 5 m with open horizontal boundary conditions. The computational domain covers −300 m ≤ x ≤ 2260 m, −160 m ≤ y ≤ 160 m, and 0 ≤ z ≤ 320 m.

The turbine-induced forces F in Equation 4 are parametrized with the blade element momentum method as rotating actuator disc with a rather large nacelle, covering 20% of the blades, to avoid any kind of instabilities in the numerical model (Englberger and Dörnbrack[35]; ED17). The tower is not considered, as it is not the major source of turbulence. The wind-turbine forces are parameterized with the airfoil data from the 10 MW reference wind turbine from the Technical University of Denmark (Mark Zagar, Vestas Wind Systems A/S; personal communication), whereas the radius of the rotor as well as the chord length of the blades are scaled to the rotor with a diameter of 100 m. A detailed description of the wind-turbine parametrization and the applied smearing of the forces, as well as all values used in the wind-turbine parametrization, are given as parametrization B in ED17.

The background flow with vertical wind shear is extracted from an equilibrium state of a neutral boundary layer precursor simulation as described in ED17. The background turbulence level is controlled via the turbulence preserving method from ED17. This method maintains the turbulence of the background flow for wind-turbine simulations with open horizontal boundaries, without the necessity of the permanent import of turbulence data from a precursor simulation, which is connected with a negligible memory requirement. The turbulence level is determined by the factor α representing the amplitude of background turbulence (cf Equation 5 in ED17). The factor α intensifies the background turbulence. In the present study, the factor α is varied in the experimental cases S8 and S9.

Large-eddy simulations of the flow offer single turbulent situations of the wind fields at individual time steps (snapshots) as well as mean values. All simulations are performed for 20 minutes, a period long enough for the wake to reach an equilibrium state with statistical convergence of the results, with one snapshot stored every minute for each case. All mean values are averaged over the last 10 minutes. The temporal average of each quantity is calculated online in the numerical model EULAG and updated at every time step according to the method of Fröhlich[36] (Equation 9.1). The mean values and altogether 21 snap shots were stored for each case for subsequent use.

Figure 2 shows how the wind turbine and the hill affect the mean flow separately in a cross-section through y_0 along the x-axis. The wind turbine rotor causes a wake with a tube-like zone with reduced wind velocity in the downwind domain of the turbine (case S0.1, Figure 2A). Closely behind the turbine, the wind is slightly accelerated above and below the wake leading to strong vertical wind velocity gradients which control the downward and upward refraction of sound waves. Note that the wake flow is a 3-dimensional feature with radial gradients at its lateral boundaries. The influence of the hill (case S1.0, Figure 2B) results in an acceleration of the air flow above the hill. The wind speed maximum is symmetrical with respect to the hill centre because the atmosphere is assumed to be neutrally stratified so that buoyancy effects do not occur.

Figure 3 shows the influences of both turbine and hill in combination (case S1, Figure 3A). The hill leads to an increased wind speed above the hill. A wind turbine placed on the hill thus experiences the intensified wind speed. This has an influence on the wake as a comparison between Figures 2A and 3A reveals. The wind speed reduction in the wake is smaller, and the wind maximum between ground and wake is intensified. The axis of the wake (height of minimum wind speed) slightly drops at the lee side of the hill but the distance from the ground surface is higher than in the case without hill.

Figure 3B presents one selected turbulent snapshot. Comparing the turbulent field in Figure 3B with the mean field in Figure 3A gives an impression how the random distribution of turbulent eddies superimposes the smooth structure of the mean wind gradients.

4 | ACOUSTICAL SIMULATIONS

4.1 | Model

Wind turbines are elevated sound sources which can be perceived over a rather wide range of several hundreds of metres up to 1 km or even more. Therefore, an efficient 3-dimensional sound propagation model is needed which accounts for 3-dimensional inhomogeneities in the air (influence of the hill and the wake of the turbine) and the effects of the uneven ground. In this study, a 3-dimensional ray-based sound particle model is used.[37] This type of model is much less expensive than a 3-dimensional time-domain Euler model, for instance. Therefore, it can be applied to a high number of situations and a rather large range. Heimann and Gross[37] compared the model with analytical results and published benchmark results of a fast-field-programme model. The model was previously applied to wind turbine noise by Heimann et al.[15]

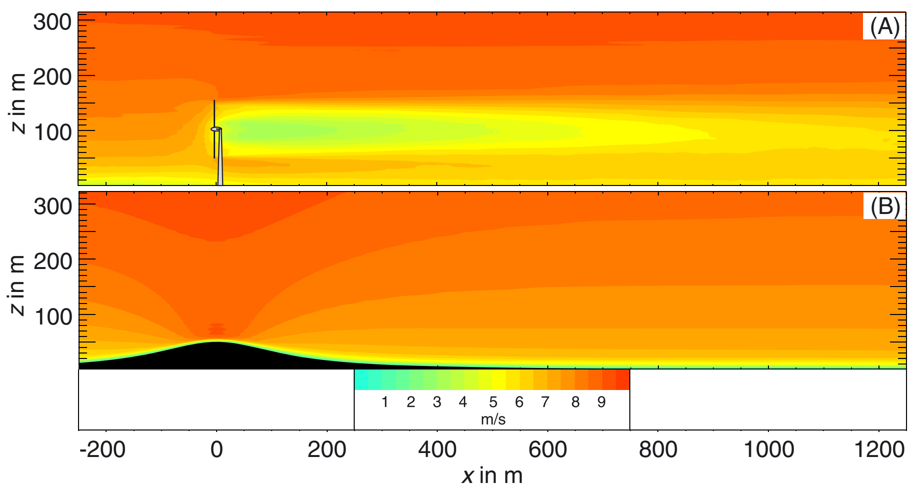

FIGURE 2 Simulated mean wind speed for the cases A, S0.1 with wind turbine and without hill and B, S1.0 with hill and without turbine [Colour figure can be viewed at wileyonlinelibrary.com]

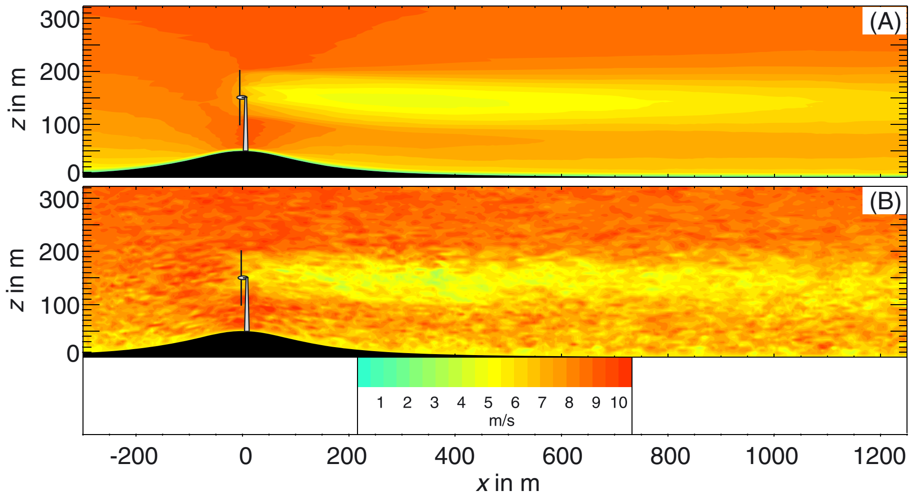

FIGURE 3 A, Simulated mean wind speed and B, one instantaneous turbulent situation for the case S1 with a wind turbine on the top of the hill [Colour figure can be viewed at wileyonlinelibrary.com]

In the model, a greater number of so-called sound particles are uniformly released at the position of one or several source points from where they propagate into the surrounding airspace. Each particle carries a certain amount of sound energy depending on the strength of the source and the starting direction to account for the source directivity. The particles travel with the effective speed of sound along rays which can be curved according to the local vertical and horizontal gradients of the sound and wind speed (refraction). The ray coordinates are calculated by a time integration of the following equations which determine the position and the direction of travel of the particles (Pierce[38]; Chapter 8):

$$\frac{dx_i}{dt} = u_i + cn_i, \tag{6}$$

$$\frac{dn_i}{dt} = -\frac{\partial c}{\partial x_i} - \sum_{j=1}^{3}\left(n_j \frac{\partial u_j}{\partial x_i}\right), \tag{7}$$

x_i (with i = 1, 2, 3 referring to the coordinates x, y, z, respectively) are the components of the position vector and n_i are the components of the wave vector which is perpendicular to the wave front and determines the direction of the particle movement. The sound speed c is a function of the local temperature T.

$$c = \sqrt{\frac{c_p}{c_v} R_d T}, \tag{8}$$

where c_p and c_v are the specific heat capacities of air at constant pressure and volume, respectively, and R_d is the gas constant of dry air. The wind components u_i in Equations 6 and 7 and the temperature T are taken from the 3-dimensional LES model output after interpolation to the current position of the sound particles.

During their travel in air, the particles continuously lose sound energy due to air absorption. This process is parameterized according to ISO 9613-1 as a function of frequency and temperature T.[39] The relative humidity is assumed to be 70%. Particles which hit the ground are reflected, ie, they change their direction (specular reflection), lose a part of their energy and change their attributed phase according to the complex impedance of the ground Z_G, the grazing angle ϕ, and the plane-wave reflection coefficient:

$$R = \frac{\sin\phi - \beta}{\sin\phi + \beta} \quad \text{with} \quad \beta = \frac{\rho c}{Z_G}, \tag{9}$$

where $\rho = p_0(R_d T)$ is the density of air. The impedance ratio β is parameterized by the flow resistivity of the ground σ and the frequency according to Delany and Bazley,[40] with σ = 300 kPa s m^{-2} in the whole domain and for all cases.

Equations 6 and 7 are solved numerically with forward-in-time differences. The sound energy of passing particles is added within defined receiver volumes considering their actual phase. The total number of particles must be chosen large enough to ensure that sufficient particles pass even remote receiver volumes to achieve statistically robust results. The specific model set-up is provided in Section 4.2.

The computational efficiency of the ray-based sound particle model is an important advantage if a set of several 3-dimensional simulations over irregular terrain and in an inhomogeneous atmosphere is envisaged. Another advantage of the Lagrangian concept is the easy implementation of the source directivity and the identification of the contribution of partial sources at the receiver.

However, there are also shortcomings. The ray theory is a high-frequency approach so that the results for low-frequency sound can be inaccurate if strong refraction plays a role. The treatment of diffraction is another weakness of ray-based models. However, in the present study, diffraction in shadows behind topographical features or refractive shadows are of minor importance because the source position is rather high and no part of the ground surface is shaded by the hill.

4.2 | Simulation set-up

Twenty-four source points are defined to represent the full sound emission during a full rotation of the rotor. The source points are 5 m away from the blade tip positions. Six source points are combined to represent 1 of 4 source quadrants (upper, downward, lower, and upward quadrant), where the terms "downward" and "upward" refer to the respective direction of motion of the rotating blades (Figure 4). The emission sound power is identical in all cases, because only propagation effects are of interest here. Relative levels are used for comparisons between the cases of Table 1. The considered frequencies cover all 1/3 octave bands from 20 Hz to 16 kHz. The emission spectrum corresponds to Deutsche WindGuard.[41] The source points are assumed to be incoherent so that the phase can be disregarded when the sound level is determined in the receiver volumes.

The directivity of the source is set according to Ffowcs Williams and Hall[42] as cited by Oerlemans.[43] In this approach, the directivity does not depend on frequency.

$$\Delta L_{\mathrm{dir}} = 10\,\mathrm{lg}\left(\sin^2(0.5\,\vartheta)\ \sin(\phi)\right) \tag{10}$$

with

$$\phi = \mathrm{acos}(-(w_x\, b_{21} + w_y b_{22} + w_z b_{23})),$$

$$\vartheta = \pi - \mathrm{acos}(-(w_x\, b_{11} + w_y b_{12} + w_z b_{13})),$$

$$b_{11} = 0; b_{12} = \cos(\gamma); b_{13} = \sin(\gamma),$$

$$b_{21} = 0; b_{22} = -b_{13}; b_{23} = b_{12},$$

$$\gamma = \mathrm{acos}\left(\frac{z - z_{hub}}{r_s}\right).$$

z is the actual height of the source, z_{hub} the hub height, and r_s is the distance between the source point and the hub with r_s = 0.9 r, where r is the radius of the rotor. The unity vector $\vec{w} = (w_x, w_y, w_z)$ defines the direction of emission, ie, it is the starting vector of a sound ray.

The necessary number of sound particles depends on the domain size, the size of the receiver volumes, and the requested accuracy of the results. Since the processing time is proportional to the number of particles, the choice of the parameters is a compromise. In this study, the domain size is confined by $0 \le x \le 1000$ m (length), -150 m $\le y \le +150$ m (width), and $0 \le z - h \le 200$ m (height). The width is limited by

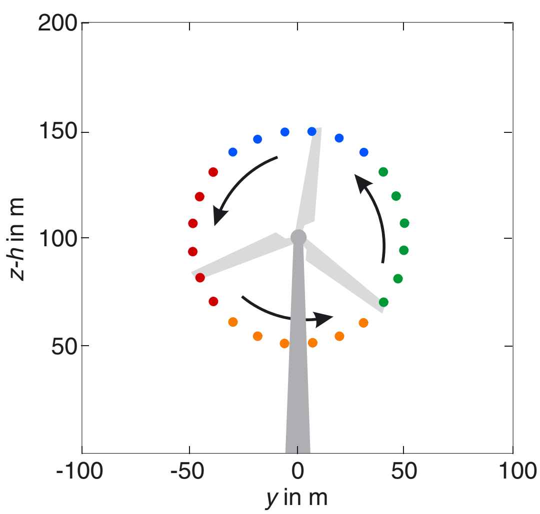

FIGURE 4 Vertical cross-section along the y-axis (at $x = x_0$) showing the wind turbine as seen from the downwind side. The coloured dots mark the 24 point sources of aerodynamic blade-tip noise. The colours indicate the 4 emission quadrants (blue: upper quadrant, red: downward quadrant, orange: bottom quadrant, green: upward quadrant) [Colour figure can be viewed at wileyonlinelibrary.com]

the LES model domain. The height ensures that all particles, even those from high source positions and in downward refraction, reach the ground within the domain.

A total of 500 000 sound particles are used per source point. The sound particles are not emitted into the full space but only into those directions that send the particles towards receiver volumes above the area 200 m ≤ x ≤ 1000 m and −150 m ≤ y ≤ + 150 m. Receivers closer than 200 m to the turbine are not considered because there are normally no dwellings. Depending on the source position, the starting direction of the particles (relative to the x-axis) ranges between −64.5° and +64.5° horizontally and between −55.4° and +27.6° vertically. The particles are traced with a time step of t = 0.003 s until they have left the computational domain. For a sound speed of c = 340 m/s, this corresponds to spatial steps of 1 m length. The spherical receiver volumes have a diameter of 5 m. The volume centres are equidistant with a spacing of x_i = 5 m.

These specifications avoid a needlessly high number of sound particles in total but still ensure that at least 100 sound particles pass through even remote receiver volumes leading to a numerical accuracy of 1% or a resolution of 0.043 dB. The accuracy of the numerically determined ray position is the lower the longer the travel distance, the larger the time step and the stronger the encountered gradient of the effective sound speed $\nabla c_{eff} = \nabla(c + u)$. Given a uniform gradient of $\nabla c_{eff} = 0.05\ s^{-1}$, leading to circular sound rays, the numerically calculated ray position at a range of 1 km from the source deviates from the analytically calculated one by only 0.2 m. In the studied cases, $|\nabla c_{eff}| \leq 0.05\ s^{-1}$ is valid in more than 95% of the model domain. Hence, the expected deviation can be estimated to be at least one order of magnitude smaller than the size of the receiver volumes.

The evaluation of the results refers to the A-weighted sound levels averaged over at least one full rotation of the rotor (referred to as long-term sound level in the following). The partial contributions from the emission quadrants (cf Figure 4) are discussed to better understand the variation of the long-term levels from case to case. The results are shown in horizontal (x-y-plane) or vertical (x-z-plane) cross-sections or as distance profiles where the results are horizontally averaged within annuli around the foot of the hub (at $x = y = 0$). The annuli are confined by the lateral domain boundaries −150 m ≤ y ≤ + 150 m. They are shown in Figure 5 where the horizontal distance s from the foot of the hub is indicated in units of the rotor diameter D. If not stated otherwise, the acoustic model results refer to the near-ground receivers with a centre height of $z - h$ = 2.5 m above ground.

4.3 | Consideration of turbulence

The influence of turbulence on sound propagation can be considered by the model in 2 ways.

Method 1: The acoustical model can be applied to a greater number of different "frozen" turbulent wind and temperature fields, ie, snapshots of the unsteady output of the LES. However, this is rather expensive because it requires a corresponding number of acoustical simulations. The entirety of simulations provides the variability of the sound level due to turbulence. The results can be averaged to an energy-equivalent mean sound level.

Method 2: The acoustical simulation is performed on the base of the mean meteorological fields and the total TKE of the flow is used to generate synthetic turbulent deviations from the mean that randomly change during the travel time of sound particles. The turbulent fields locally fulfil the TKE as it resulted from the LES. The size distribution of the generated eddies corresponds to the Prandtl spectrum of turbulence. This procedure was proposed and tested by Heimann and Blumrich[44] to save storage and processing time in the application of a finite-difference time-domain model. It is here implemented in the sound particle model.

To document how both methods affect the results of the sound propagation simulation, a comparison was performed. For case S1, propagation simulations were run separately for all stored 21 snapshots and the results were subsequently averaged (Method 1). This result was compared with the result of one propagation simulation based on the mean wind field which is successively superimposed by 21 synthetically generated turbulence realizations (Method 2). Figure 6 shows this comparison. The calculated mean sound level profiles (the 2 bold curves) do merely deviate by 0.3 dB in average. Therefore, to minimize the computational effort, all subsequent sound propagation simulations were made with Method 2, ie, one simulation instead of 21 per case.

5 | RESULTS

Numerical experimentation allowed for separating the influences of the inflow condition, the hill geometry, and the downwind wake. Moreover, it was possible to identify the respective contributions of the 4 emission quadrants to the sound level.

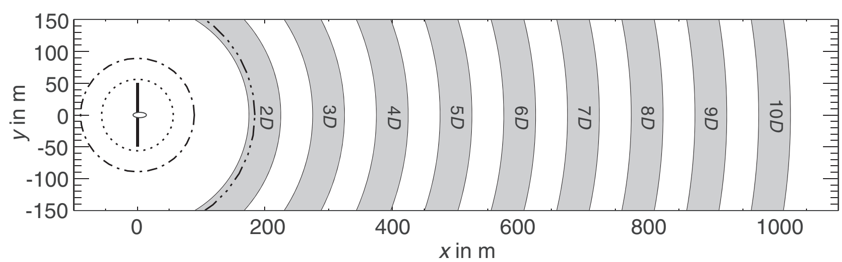

FIGURE 5 Downwind domain of the wind turbine. The results of the sound propagation model are evaluated in the grey-shaded segments representing different horizontal distances from the hub position in terms of the rotor diameter D. The circles around (x_0 = 0, y_0 = 0) represent the H/2-isohypses of the terrain elevation h for maximum slope angles φ = 30° (dotted), φ = 20° (dash-dot), and φ = 10° (dash-3dots)

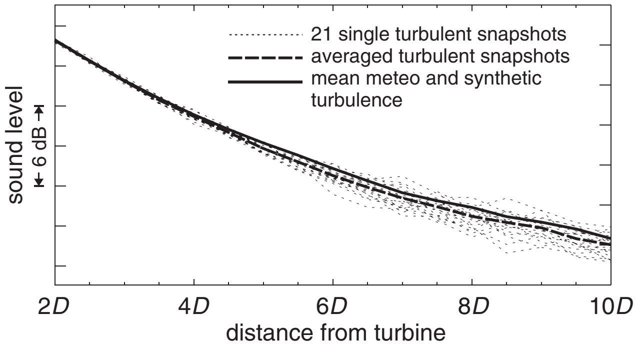

FIGURE 6 Simulated A-weighted sound level for case S1 averaged within the annuli shown in Figure 5 with different treatment of turbulence as indicated

The sound propagation in the downstream domain of the wind turbine is influenced by the 2 modifications of the wind field: the wake and the hill effect. The wake consists of a tube-like zone behind the rotor with reduced wind speed (Figure 3A). It leads to refraction of soundwaves towards the centre of the tube and thus forms a duct for sound waves that enter the wake with a small angle. Since the vertical wind gradient is normally larger at the top boundary of the wake than at its bottom, downward refraction above the wake axis is stronger than upward refraction below this axis. This effect is expected to increase the sound level near the ground at larger distances in the downwind domain (see also Heimann et al[15]). If the wind turbine stands on top of a hill, the slant distance between the rotor and the plane ground level farther away is increased and the near-ground sound level is therefore expected to be decreased. On the other hand, the hill causes an acceleration of the wind which enhances the downward refraction in the downwind regime (Figure 2B). The latter would rather tend to increase the near-ground sound level.

The main features of sound propagation from a hilltop wind turbine through its wake leeside of the hill are discussed by the example of case S1. Figure 7 shows the effect of refraction on the sound level at the near-ground receivers, ie, the difference between the sound level of case S1 and the sound level that resulted from a "no refraction" control run with switched-off refraction (straight rays) but the same conditions otherwise. In areas with a positive difference, refraction has caused a surplus in sound energy either by ray convergence (focussing) or less divergence than in the "no refraction" control case. Vice versa, in areas with a negative difference, refraction has caused a deficit in sound energy either by shadow forming near the ground or stronger divergence than in the "no refraction" control case.

The most striking feature in Figure 7 is the intensification by refraction for sound emerging from the upper emission quadrant and a corresponding weakening for sound from the lower emission quadrant. The highest values are found near the centre line for $x \geq 800$ m = 8*D*. The reason for this behaviour is the downward refraction at the upper boundary of the wake and the upward refraction at the lower boundary. The vertical cross-sections of sound levels relative to "no refraction" in Figure 8 underline this effect. The 3-dimensional geometry of the wake flow (cf Figure 3) leads to a focussing of sound from the upper emission quadrant which increasingly affects lower layers with growing distance. Sound from the lower emission quadrant is upward refracted so that a shadow forms and less sound energy reaches the lower layers at greater distance.

The total sound impact at receivers is determined by the superimposition of the sound emitted by all 3 rotating blades. The sound ray path from each blade position to a receiver starts with a specific directivity, is varyingly long, and experiences specific refraction. Among other effects, this causes the locally received sound level to vary as the blades rotate. The behaviour is known as "amplitude modulation," and it is supposed to be quite annoying.[45] Near the turbine, the rather wide range of involved emission angles (directivities) and source-receiver distances mainly contributes to this modulation. Further away refraction dominates the modulation as the different contributions of the emission quadrants suggest (Figures 7 and 8).

Figure 9 shows this variation during a full rotation for the cases S0.1 (no hill) and S1 (with hill). In either case, 12 simulations were performed with 3 concurrently emitting blade tips. The rotor is turned by 10° from one simulation to the next one. The sound-level variation increases with growing distance from the turbine. It is slightly higher in the case with hill where sound-level amplitude reaches almost 5.4 dB at $s = 10\,D$ distance, but only 4.0 dB without hill. The magnitude agrees with measurements by Larsson and Öhlund[46] about 1 km away from wind turbines located on a hill in the Dragaliden site in Sweden. Note that the curves in Figure 9 refer to the indicated rotor angle. They do not exactly represent the temporal behaviour at the receivers since synchronously emitted sound at the 3 blades may need different travel times towards the receiver.

The results of all cases are presented in Figure 10 as distance-dependent profiles of the A-weighted sound level. The findings from this graph are

1. The contribution of the lower and downward emission quadrant to the near-ground sound level is higher than the contribution by the other 2 quadrants for $s \leq 4\,D$. This results from the higher slant distance between the upper emission points and the ground and by directivity effects.
2. The long-term sound level is dominated by the contribution from the downward emission quadrant close to the turbine $s \leq 4\,D$ and by the emission from the upper quadrant farther away for $s \geq 6\,D$.

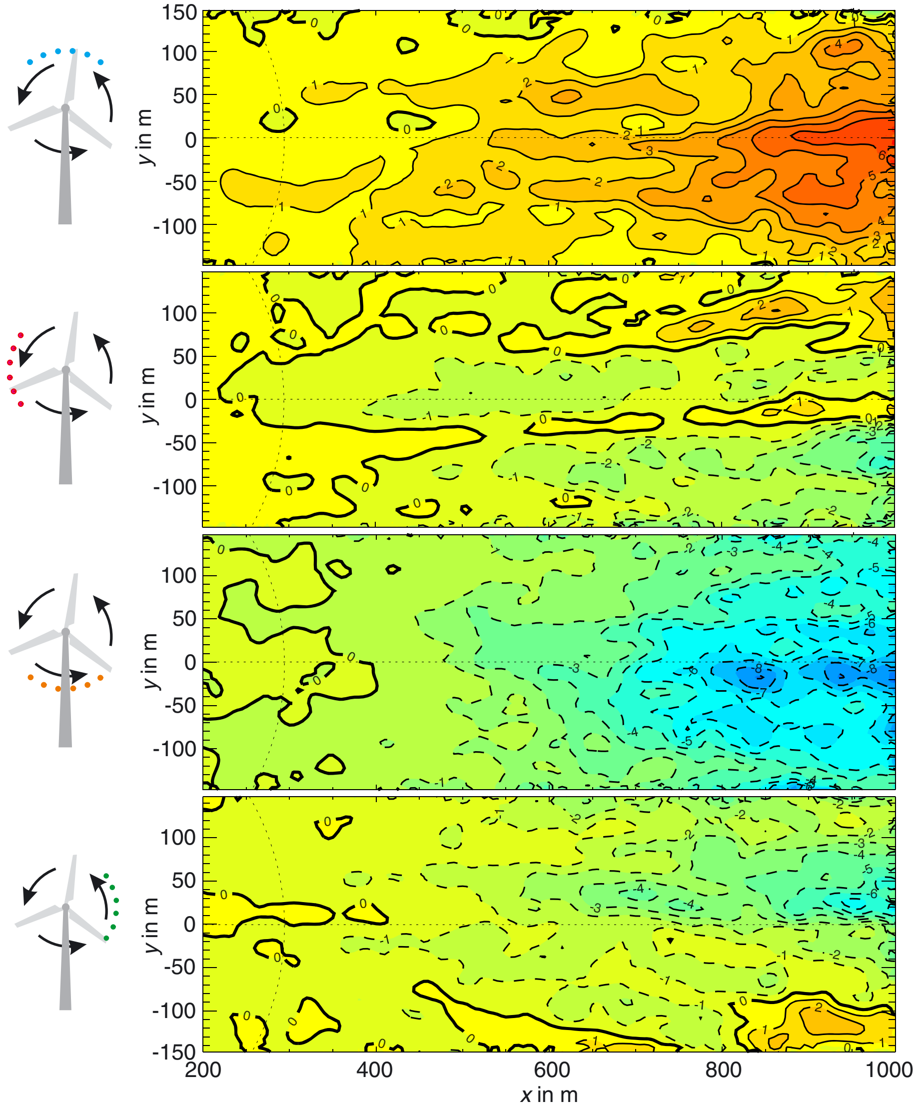

FIGURE 7 Near-ground sound level relative to "no refraction" for case S1(with hill) averaged over one full rotation. The wind turbine is located at $x = y = 0$. The results of the 4 panels refer to the emission quadrants as sketched on the left [Colour figure can be viewed at wileyonlinelibrary.com]

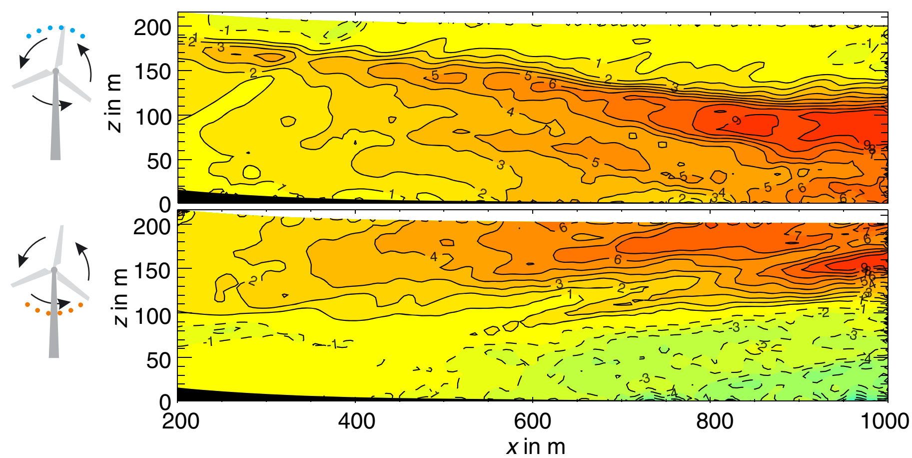

FIGURE 8 Vertical cross-sections along the x-axis (at $y = y_0$) of the sound level relative to "no refraction" as simulated for case S1 (with hill, $\varphi = 10^{\circ}$). The upper and lower panels show the results for the upper and lower emission quadrant, respectively. The wind turbine is located at $x = y = 0$ [Colour figure can be viewed at wileyonlinelibrary.com]

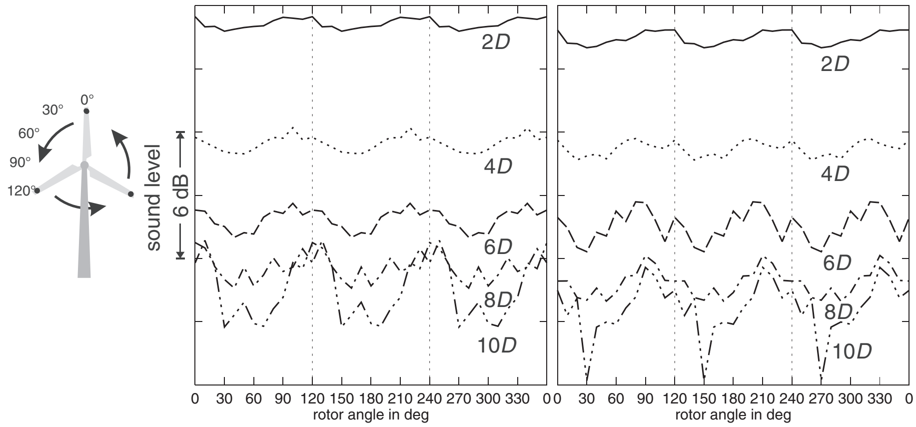

FIGURE 9 Near-ground sound level as a function of the rotor angle at the time of emission. The curves refer to the downwind annuli 2*D*, 4*D*, etc, within the stripe −50 m ≤ *y* ≤ + 50 m. Left panel: case S0.1 (no hill), right panel: case S1 (with hill)

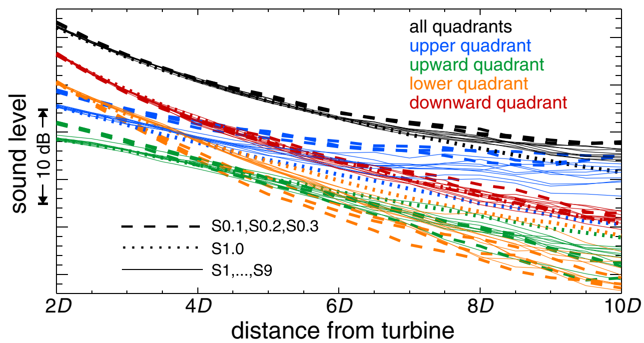

FIGURE 10 Simulated A-weighted sound levels for all cases (as indicated) averaged within the annuli shown in Figure 5. Colours show the contribution of emission quadrants. The black curves refer to the long-term sound level (all quadrants; mean over a full rotation) [Colour figure can be viewed at wileyonlinelibrary.com]

3. The emission from an elevated source on top of a hill (cases S1 … 9 vs S0.x) leads to lower sound levels for emissions from the upper quadrant within 2*D* ≤ *s* ≤ 10*D*. It leads to lower levels for emissions from the upward quadrant only near the source *s* ≤ 4*D* and it leads to higher levels for emissions from the lower quadrant for medium distances (3*D* ≤ *s* ≤ 7*D*). This is partly caused by the slant distance which is somewhat higher in the case with hill. Also, the directivity has an influence because rays with steeper starting angles reach the receivers.
4. The highest long-term sound levels are calculated for the cases without a hill (S0.x) and the lowest one for the case without a wake (S1.0). This means that the position of the wind turbine on top of the hill slightly reduces the sound level, while the wake increases it.
5. If the wake is disregarded (case S1.0), the emission quadrant does not play a major role beyond *s* ≥ 6*D*. This underlines the importance of refraction at the lower and upper boundary of the wake once it exits.
6. The long-term sound level (sound from all emission points averaged over a full rotation) is almost independent of the cases S1 … S9 near the source *s* ≤ 6 *D*. Even at *s* = 10*D*, the cases differ by only 3 dB. Apparently, the opposing effects on the sound emerging from the lower and upper emission quadrants do almost completely compensate.

Figure 11 provides an overview of the effects of parameter variations between the cases on the mean sound level (full rotation). The cases S0.1, S0.1, and S0.3 with a turbine on flat ground show the highest near-ground sound levels for the range *s* > 6*D*. In the same range, the negligence of the wake (case S1.0) results in the lowest sound level. The variations of the surface roughness length z_o, the steepness of the hill φ, the friction velocity u_*, and the turbulence level α (cases S1 … S9) only lead to small changes of the sound level of less than 1 dB. Nevertheless, it is noticeable that the order of the effects partly varies with distance. For example, the flat hill (case S1; $\varphi = 10^{\circ}$) has the lowest sound level of the cases S1, S2, and S3 at *s* = 4*D*, while it has the highest one at *s* = 10*D*. At *s* = 10*D*, the result of S2 is lower than the results of S1 and S3 although the steepness of the hill steadily increases from S1 to S2 and to S3. This behaviour is caused by the superimposition of reflection and refraction effects and the fact that the reflection angle is very sensitive to variations of the ground surface profiles and the position of convex and concave terrain segments. A change in order can be also observed for the variation of u_* (cases S6 and S7), while the influences of the variations of z_0 and α do not change the order.

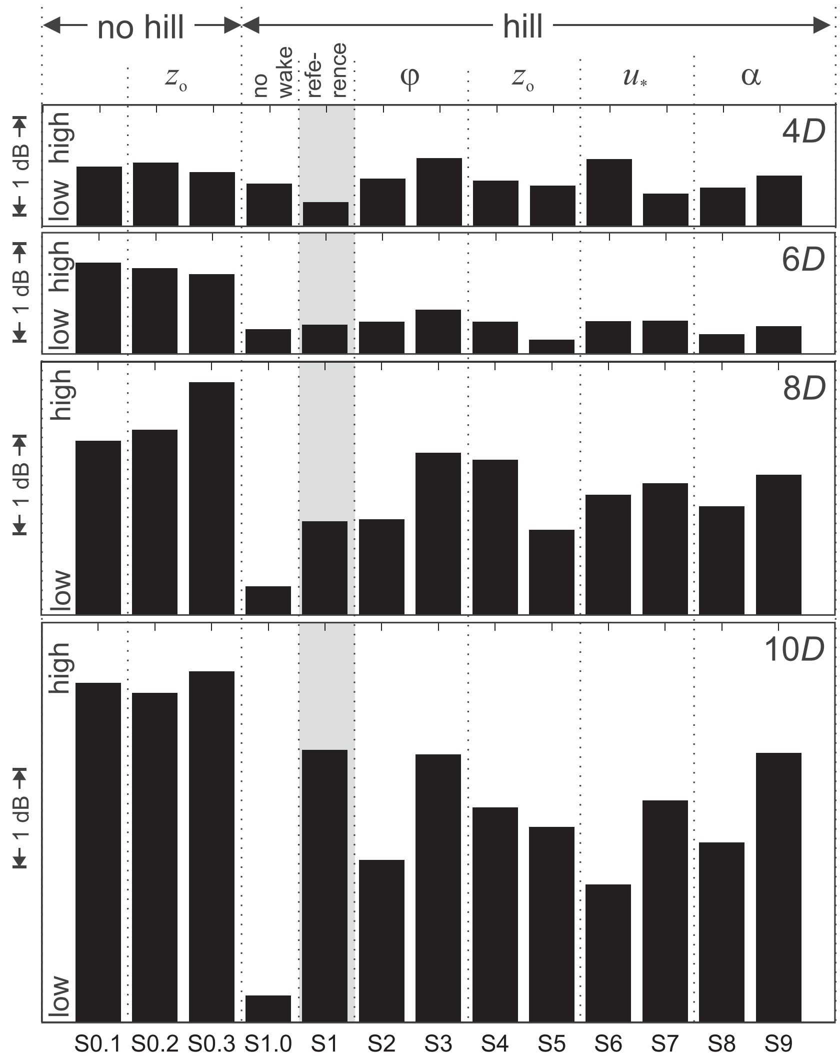

FIGURE 11 Simulated long-term A-weighted sound levels (all emission quadrants, mean over a full rotation) averaged within the 4*D*, 6*D*, 8*D*, and 10*D* annuli (cf Figure 5) for all cases. On the top it is indicated which parameters are varied (cf Table 1)

6 | DISCUSSION AND CONCLUSION

The sound impact of a wind turbine located on the top of a hill was investigated by means of numerical simulation. The study investigated the combined effects of the hill geometry, its influence on the wind field (including turbulence), and the wake of the rotor. The numerical approach allowed to separate single effects and to vary further parameters which govern the 3-dimensional structures of the airflow.

As a general finding of the study, it can be stated that there is only a weak influence of the parameter variations on the A-weighted near-ground mean sound levels. If the turbine is positioned on top of a 50 m high hill instead of flat terrain, the sound level is reduced by 1 to 2 dB in the range $s > 6D$. This reduction partly compensates the increase in sound level by 2 to 4 dB due to the refraction at the shear zones of the always existing wake. Variations of the maximum hill slope angle $10^\circ \le \varphi \le 30^\circ$, the surface roughness 0.05 m $\le z_0 \le$ 0.2 m (controlling the vertical inflow wind shear), friction velocity 0.3 m/s $\le u_* \le$ 0.6 m/s (controlling the inflow wind speed), and inflow turbulence level $5 \le \alpha \le 20$ have a rather marginal effect on the near-ground sound level of merely 1 dB at $s = 10\,D$.

It has to be noted that the numerical experiments are limited to adiabatic, ie, statically neutral, stratification. Especially, nighty situations with a combination of stable stratification and the formation of a low-level jet, ie, positive vertical gradients of the sound speed together with strong wind speed gradients, are supposed to enhance downward refraction resulting in higher sound levels.

In this study, only propagation effects are compared, because the same emission strength was assumed in all 13 cases. In reality, the sound emission also depends on the rotor speed, which in turn is determined by the wind speed impinging the rotor plane. If the turbine stands on a hill, the simulations suggest that geometrical effects and the refraction due to the specific airflow modifications by hill and rotor increase the propagation loss in the downwind domain. However, the therefore expected reduction of the sound impact might be partly compensated by the fact that the wind speed above the hill is increased, the turbine rotates faster, and the sound emission is correspondingly higher.

ACKNOWLEDGEMENTS

This research was performed as part of the LIPS project, funded by the German Federal Ministry for Economic Affairs and Energy under grant no. 0325518 by a resolution of the German Federal Parliament. The authors gratefully acknowledge the Gauss Centre for Supercomputing e.V. (www.gauss-centre.eu) for supporting this project by providing computing time on the GCS Supercomputer SuperMUC at Leibniz Supercomputing Centre (LRZ, www.lrz.de).

ORCID

Arthur Schady http://orcid.org/0000-0002-3078-9546

REFERENCES

1. Kim H, Lee S, Son E, Lee S, Lee S. Aerodynamic noise analysis of large horizontal axis wind turbines considering fluid–structure interaction. *Renew Energy*. 2012;42:46-52. https://doi.org/10.1016/j.renene.2011.09.019
2. Rogers AL, Manwell JF, Wright S. Wind turbine acoustic noise. A white paper prepared by Renewable Energy Research Laboratory, University of Massachusetts 2006; Obtainable from http://www.ceere.org.
3. Tabassum-Abbasi, Premalatha M, Abbasi T, Abbasi SA. Wind energy: increasing deployment, rising environmental concerns. *Renew Sustain Energy Rev*. 2014;31:270-288. https://doi.org/10.1016/j.rser.2013.11.019
4. Pedersen E, van der Berg F, Bakker R, Bouma J. Response to noise from modern wind farms in The Netherlands. *J Acoust Soc Am*. 2009;126:634-643. https://doi.org/10.1121/1.3160293
5. Vermeer LJ, Sørensen JN, Crespo A. Wind turbine wake aerodynamics. *Prog Aerosp Sci*. 2003;39:467-510. https://doi.org/10.1016/S0376-0421(03)00078-2
6. Bingöl F, Mann J, Larsen GC. Light detection and ranging measurements of wake dynamics. Part I: one-dimensional scanning. *Wind Energy*. 2010;13:51-61. https://doi.org/10.1002/we.352
7. Trujillo JJ, Bingöl F, Larsen GC, Mann J, Kühn M. Light detection and ranging measurements of wake dynamics. Part II: two-dimensional scanning. *Wind Energy*. 2011;14:61-75. https://doi.org/10.1002/we.402
8. Käsler Y, Rahm S, Simmet R. Wake measurements of a multi-MW wind turbine with coherent long-range pulsed Doppler wind lidar. *J Atmos Oceanic Tech*. 2010;27:1529-1532. https://doi.org/10.1175/2010JTECHA1483.1
9. Wussow S, Sitzki L, Hahm T. 3D-simulations of the turbulent wake behind a wind turbine. *J Phys Conf Ser*. 2007;75:012033. https://doi.org/10.1088/1742-6596/75/1/012033
10. Jimenez A, Crespo A, Migoya E, Garcia J. Advances in large-eddy simulation of a wind turbine wake. *J Phys Conf Ser*. 2007;75:012041. https://doi.org/10.1088/1742-6596/75/1/012041
11. Troldborg N, Sørensen JN, Mikkelsen R. Numerical simulations of wake characteristics of a wind turbine in uniform inflow. *Wind Energy*. 2010;13:86-99. https://doi.org/10.1002/we.345
12. Gross G. Numerical simulations to the diurnal variation of wakes behind wind turbines. *Meteorol Z*. 2010;19:91-99. https://doi.org/10.1127/0941-2948/2010/0418
13. Sørensen JN, Mikkelsen RF, Henningson DS, Ivanell S, Sarmast S, Andersen SJ. Simulation of wind turbine wakes using the actuator line technique. *Phil Trans R Soc A*. 2015;373:20140071. https://doi.org/10.1098/rsta.2014.0071
14. Gebraad PMO, Teeuwisse FW, van Wingerden JW, et al. Wind plant power optimization through yaw control using a parametric model for wake effects—a CFD simulation study. *Wind Energy*. 2016;19:95-114. https://doi.org/10.1002/we.1822
15. Heimann D, Käsler Y, Gross G. The wake of a wind turbine and its influence on sound propagation. *Meteorol Z*. 2011;20:449-460. https://doi.org/10.1127/0941-2948/2011/0273
16. Lee S, Lee D, Honhoff S. Prediction of far-field wind turbine noise propagation with parabolic equation. *J Acoust Soc Am*. 2016;140:767-778. https://doi.org/10.1121/1.4958996
17. Barlas E, Zhu WJ, Shen WZ, Kelly M, Andersen SJ. Effects of wind turbine wake on atmospheric sound propagation. *Appl Acoust*. 2017;122:51-61. https://doi.org/10.1016/j.apacoust.2017.02.010
18. Corby GA. The airflow over mountains—a review of the state of current knowledge. *Quart J R Met Soc*. 1954;80:491-521.
19. Davidson B, Gerbier N, Papagionakis SO, Rijkoort PG. Sites for wind power installations, World Meteorological Organisation. *Tech Note*. 1964;63.
20. Taylor PA. Some numerical studies of surface boundary-layer flow above gentle topography. *Bound-Layer Meteorol*. 1977;11:439-465.
21. Taylor PA, Teunissen HW. The Askervein Hill project: overview and background data. *Bound-Layer Meteorol*. 1987;39:15-39. https://doi.org/10.1007/BF00121863
22. Berg J, Mann J, Bechmann A, Courtney MS, Jørgensen HE. The Bolund experiment, part I: flow over a steep, three-dimensional hill. *Bound-Layer Meteorol*. 2011;141:219-243. https://doi.org/10.1007/s10546-011-9636-y
23. Conan B, Chaudhari A, Aubrun S, van Beeck J, Hämäläinen J, Hellsten A. Experimental and numerical modelling of flow over complex terrain: the Bolund hill. *Bound-Layer Meteorol*. 2016;158:183-208. https://doi.org/10.1007/s10546-015-0082-0
24. Lundtang Petersen E, Troen I, Ejsing Jørgensen H, Mann J. The new European wind atlas. *Energy Bulletin*. 2014;17:34-39.
25. Prospathopoulos JM, Voutsinas SG. Application of a ray theory model to the prediction of noise emissions from isolated wind turbines and wind parks. *Wind Energy*. 2006;10:103-119. https://doi.org/10.1002/we.211
26. Van Renterghem T. Sound propagation from a ridge wind turbine across a valley. *Phil Trans R Soc A*. 2017;375:20160105. https://doi.org/10.1098/rsta.2016.0105
27. Prusa JM, Smolarkiewicz PK, Wyszogrodzki AA. EULAG, a computational model for multiscale flows. *Computers & Fluids*. 2008;37:1193-1207. https://doi.org/10.1016/j.compfluid.2007.12.001

28. Smolarkiewicz PK, Margolin LG. MPDATA: a finite-difference solver for geophysical flows. *J Comput Phys*. 1998;140:459-480.
29. Smolarkiewicz PK, Sharman R, Weil J, Perry SG, Heist D, Bowker G. Building resolving large-eddy simulations and comparison with wind tunnel experiments. *J Comput Phys*. 2007;227:633-653. https://doi.org/10.1016/j.jcp.2007.08.005
30. Kühnlein C, Smolarkiewicz PK, Dörnbrack A. Modelling atmospheric flows with adaptive moving meshes. *J Comput Phys*. 2012;231:2741-2763. https://doi.org/10.1016/j.jcp.2011.12.012
31. Smolarkiewicz PK, Prusa JM. Towards mesh adaptivity for geophysical turbulence: continuous mapping approach. *Int J Numer Methods Fluids*. 2005;47:789-801. https://doi.org/10.1002/fld.858
32. Wedi NP, Smolarkiewicz PK. Extending Gal-Chen and Somerville terrain-following coordinate transformation on time-dependent curvilinear boundaries. *J Comput Phys*. 2004;193:1-20. https://doi.org/10.1016/j.jcp.2003.07.034
33. Margolin LG, Smolarkiewicz PK, Sorbjan Z. Large-eddy simulations of convective boundary layers using nonoscillatory differencing. *Physica D: Nonlinear Phenomena*. 1999;133:390-397.
34. Schmidt H, Schumann U. Coherent structure of the convective boundary layer derived from large-eddy simulations. *J Fluid Mech*. 1989;200:511-562.
35. Englberger A, Dörnbrack A. Impact of neutral boundary-layer turbulence on wind-turbine wakes: a numerical modelling study. *Bound-Layer Meteorol*. 2017;162:427-449. https://doi.org/10.1007/s10546-016-0208-z
36. Fröhlich J. *Large Eddy Simulation Turbulenter Strömungen*. Wiesbaden: Teubner Verlag / GWV Fachverlage GmbH; 2006:414.
37. Heimann D, Gross G. Coupled simulation of meteorological parameters and sound intensity in a narrow valley. *Appl Acoust*. 1999;56:73-100.
38. Pierce AD. *Acoustics—an introduction to its physical principles and applications*. New York: McGraw-Hill Inc.; 1981:1-619.
39. ISO 9613–1. Acoustics; attenuation of sound during propagation outdoors; part 1: calculation of the absorption of sound by the atmosphere. 1993.
40. Delany ME, Bazley EN. Acoustical properties of fibrous absorbent materials. *Appl Acoust*. 1970;3:105-116.
41. Deutsche WindGuard GmbH. Schallemissionsmessungen an einer Windenergieanlage. Bericht MN15016.A1, 2015; 49 pages.
42. Ffowcs Williams JE, Hall LH. Aerodynamic sound generation by turbulent flow in the vicinity of a scattering half plane. *J Fluid Mech*. 1970;40:657-670.
43. Oerlemans S. Wind turbine noise: primary noise sources. Nationaal Luchten Ruimtevaartlaboratorium, report NLR-TP-2011–066, 2011; 57 pages
44. Heimann D, Blumrich R. Time-domain simulations of sound propagation through screen-induced turbulence. *Appl Acoust*. 2004;65:561-582. https://doi.org/10.1016/j.apacoust.2003.09.007
45. Yoon K, Gwak DY, Seong Y, Lee S, Hong J, Lee S. Effects of amplitude modulation on perception of wind turbine noise. *J Mech Sci Technol*. 2016;30:4503-4509. https://doi.org/10.1007/s12206-016-0918-7
46. Larsson C, Öhlund O. Amplitude modulation of sound from wind turbines under various meteorological conditions. *J Acoust Soc Am*. 2014;135:67-73. https://doi.org/10.1121/1.4836135

How to cite this article: Heimann D, Englberger A, Schady A. Sound propagation through the wake flow of a hilltop wind turbine—A numerical study. *Wind Energy*. 2018;21:650–662. https://doi.org/10.1002/we.2185